Design of Minimum Cost Degradation-Conscious Lithium-Ion Battery Energy Storage System to Achieve Renewable Power Dispatchability

Design of Minimum Cost Degradation-Conscious Lithium-Ion Battery Energy Storage System to Achieve Renewable Power Dispatchability

Yang Li [a], Mahinda Vilathgamuwa [b], San Shing Choi [b], Binyu Xiong [a,*], Jinrui Tang [a], Yixin Su [a], Yu Wang [c]

[a] *School of Automation, Wuhan University of Technology, 122 Luoshi Road, Hongshan District, Wuhan, Hubei 430070, China*
[b] *School of Electrical Engineering and Computer Science, Queensland University of Technology, 2 George St, Brisbane, Queensland 4000, Australia*
[c] *Rolls Royce@NTU Corporate Lab, Nanyang Technological University, 65 Nanyang Drive, Singapore 637460, Singapore*

* Corresponding author.
Email address: yang.li@whut.edu.cn (Y. Li), mahinda.vilathgamuwa@qut.edu.au (M. Vilathgamuwa), sanshing.choi@qut.edu.au (S. S. Choi), bxiong2@whut.edu.cn (B. Xiong), tangjinrui@whut.edu.cn (J. Tang), suyixin@whut.edu.cn (Y. Su), wang_yu@ntu.edu.sg (Y. Wang).

Abstract: The application of lithium-ion (Li-ion) battery energy storage system (BESS) to achieve the dispatchability of a renewable power plant is examined. By taking into consideration the effects of battery cell degradation evaluated using electrochemical principles, a power flow model (PFM) of the BESS is developed specifically for use in system-level study. The PFM allows the long-term performance and lifetime of the battery be predicted as when the BESS is undertaking the power dispatch control task. Furthermore, a binary mode BESS control scheme is proposed to prevent the possible over-charge/over-discharge of the BESS due to the uncertain renewable input power. Analysis of the resulting new dispatch control scheme shows that a proposed adaptive BESS state of energy controller can guarantee the stability of the dispatch process. A particle swarm optimization algorithm is developed and is incorporated into a computational procedure for which the optimum battery capacity and power rating are determined, through minimizing the capital cost of the BESS plus the penalty cost of violating the dispatch power commitment. Results of numerical examples used to illustrate the proposed design approach show that in order to achieve hourly-constant power dispatchability of a 100-MW wind farm, the minimum-cost Li-ion BESS is rated 31-MW/22.6-MWh.

Keywords: lithium-ion battery, renewable power dispatchability, battery degradation, battery energy storage system

1. Introduction

Non-hydro renewable energy (RE) generation such as that based on wind and solar have achieved rapid development around the world in recent years. By the end of 2018, for example, the rated wind and photovoltaic power generating capacity in the Australian states of South Australia, Victoria and Tasmania has reached some 46%, 12.1% and 11.8% of the respective state's generation capacity [1]. Unlike conventional generating units, however, such renewable generating plants cannot be dispatched flexibly due to the inherent stochastic nature of wind speed or solar irradiance. Generation reserve has to be arranged to counter the uncertain wind/solar input powers and to ensure acceptable system-level supply security and reliability are maintained. Unfortunately, this practice increases the operating costs of the power systems [2].

An alternative to the provision of generation reserve is the use of large-scale energy storage system, and lithium-ion (Li-ion) based battery energy storage system (BESS) has become a most prominent candidate for such an application [3]. This developmental trend is in some way aided by the maturity and drastic cost reduction of Li-ion battery, as is witnessed in the wide-spread application of this type of battery in electric vehicles [4]. In grid-connected application, an example is the 100-MW/129-MWh Li-ion battery station recently commissioned to operate in conjunction with the 315-MW Hornsdale wind farm in the South Australian grid system [5]. Generally BESSs are installed to undertake various tasks. Often a BESS is viewed as a power smoothing device to reduce the negative impacts the perturbing solar power [6] and wind power [7] can cause to grids, and to achieve peak shaving [8]. In distribution networks in which there are high levels of renewable penetration, BESSs can be used through distributed control to provide reactive power control [9], voltage regulation [10] as well as ancillary services to minimize the voltage deviations and losses [11]. Recently, much research attention has also been directed toward the use of BESS to achieve the dispatchability of the renewables. Different BESS configurations are designed so that renewable power plants can be dispatched in a manner very much like the conventional thermal power stations. These include dual-battery BESSs with mechanically-controlled switches [12] and with power converters [13], as well as the BESSs incorporating supercapacitor [14] or superconducting magnetic energy storages in hybrid energy storage systems [15]. In this role, the BESS is to store any surplus power from the RE generators when the produced power is higher than the predetermined and committed generation schedules. Conversely, the stored energy in the BESS can compensate for any shortfall should the generated power is less than the committed schedules. In this way, less operating generation reserve is required and the overall generation cost of the grid system can be reduced as a result. Often such a dispatchable power plant will enjoy higher tariff which will be attractive to the RE operators.

One pertinent aspect of such a RE-BESS plant is that the wind turbine generators (WTG) or the photovoltaic (PV) panels can be expected to have a lifetime considerably longer than that of a Li-ion BESS, based on current state of technological development of the electrochemical battery [16]. And yet the BESS is to play a crucial role in ensuring the dispatchability of the renewable generators throughout the lifetime of the RE power plant. With given power market rules and BESS characteristics, the design of the BESS, which involves the determination of the BESS capacity as well as the BESS

Nomenclature

AC	Annualized capital cost	$\bar{P}_g$, $\bar{P}_{g,f}$	Actual and forecasted powers generated from the renewables
AP	Annualized penalty cost	$\bar{P}_{\text{mis}}$	Mismatch between the scheduled and delivered powers
AR	Annualized replacement cost	Q_1^+, Q_1^-	Electric charges stored in the electrode (Ah)
PC	Penalty cost	Q_{loss}	Reduced capacity due to the loss of cyclable lithium ions (Ah)
TC	Capital cost	Q_{max}	Ah capacity of the battery (Ah)
C_1^+, C_1^-	Electrode capacitances (F)	R_1^+, R_1^-	Resistance of the electrode (Ω)
E_1	Stored energy (Wh)	R_{eq}	Equivalent lumped internal resistance of the battery (Ω)
E_{max}	Energy capacity of the battery (Wh)	SOE	State of energy
$\bar{E}_b$	Normalized BESS energy capacity	SOH	State of health
$\bar{E}_{\text{mis}}$	Mismatch between the scheduled and delivered energy	T_{EOL}	Lifetime of the battery (years)
I_1^+, I_1^-	Electrode currents due to the main reactions (A)	T_{RE}	Service life of the renewable plant (years)
I_{sr}	Electrode current due to the side reactions (A)	V_1^+, V_1^-	Capacitor voltages or OCPs of the electrodes (V)
I_{bat}	Applied current of the battery cell (A)	V_{bat}	Terminal voltage of the battery cell (V)
K_c	Control gain of the feedback dispatch controller	V_{OC}	Open-circuit voltage of the battery cell (V)
N_{cell}	Number of the battery cells in a BESS	$\bar{P}_g$, $\bar{P}_{g,f}$	Actual and forecasted powers generated from the renewables
P_N	Base value of the power plant (MW)	k	Index of dispatch interval
P_{bat}	Terminal power of the battery cell (W)	z	Scheduled period for which the dispatch is committed
$\bar{P}_b$	Normalized battery power	β	Binary mode coefficient
$\bar{P}_{b,\text{max}}$	Normalized power capacity of the BESS	ζ	A coefficient used to indicate the end of life of the battery
$\bar{P}_d$, $\bar{P}_{d,f}$	Actual and forecasted dispatched power	η_1	Ratio of power flow P_1 in C_1^+ and C_1^- and the power flow P_{bat}
$\bar{P}_{d,\text{adj}}$	Adjusted dispatched power	η_b, η_d, η_g	Power conversion gains of respective network components
$\bar{P}_{d,\text{sch}}$	Power schedule submitted to the grid operator	λ	Scaling factor converting power flow from battery cell to BESS
$\bar{P}_{d,\text{ref}}$	Pre-determined power to be dispatched	τ	Dispatch interval (hour)

operational strategy, can be formulated as a system-level optimization problem and in which cost-benefit analysis can be included [17]. For example, the dispatch strategy and BESS capacity are determined by maximizing a defined service lifetime/cost index, so that the short-term dispatchability of a wind farm is achieved [18]. A statistical approach to determine the capacity and the charging/discharging strategy for battery-supercapacitor hybrid storage system is proposed in [14] to achieve a dispatchable wind farm. Operational planning for a wind–battery system is carried out in [19] using a modified min-max dispatch method. A coordinated operational dispatch and capacity determination design approach for a BESS-wind farm is proposed in [20], with the view to mitigate the fluctuation and stochastic nature of the wind resources through changing the wind farm output power reference value between optimistic and pessimistic forecast scenarios. Based on Sequential Monte Carlo simulation technique, a wind farm incorporated with BESS is designed in [21] to track the generation schedule while in [22], the optimal BESS capacity and control strategy is studied by considering the real-time pricing of electricity.

In the design of the dispatchability strategy of the renewable generators described in [12-15, 18-22], the battery is modelled either by linking the battery input/output powers through some algebraic relationships, or by using an empirically-derived equivalent circuit. One major disadvantage of these models is that no insights can be gained concerning the internal states and physical limitations of the battery, e.g., the battery state of health. Furthermore, the parametric values of the models need to be adjusted because one cannot assume the performance of the BESS will remain the same throughout the lifetime of the battery. For example, chemical reactants and active materials in the battery cell do interact in the course of the usage of the battery, which will in turn lead to degraded performance of the battery over time [23]. How to adjust the parametric values to accurately reflect the condition of the battery can be most challenging. In [12-15, 18-22], when the degradation of the battery is considered, it is simply expressed in term of the expected battery lifetime, maximum charging/discharging cycle numbers, or overall Ah-throughout. The information is then used for cost/benefit analysis. Many of these empirical methods were derived based on the cycling curves which are devised to reflect the typical usage patterns specifically for mobile applications of the battery. The long-term impact of the degradation on grid-connected BESS dynamic performance has not been fully studied and indeed, standard test profiles do not exist for such grid-connected BESS. In fact, the actual physical process leading to the cell degradation cannot be readily incorporated into the empirically-derived equivalent circuit models used in these works.

In contrast, another category of the Li-ion battery models is derived from the principles of electrochemistry and thermodynamics. These models are able to describe the degradation behaviors and can be used to predict battery performance more accurately [24, 25]. However, such models are exceedingly complex as to be of practical use in power system design study. Even the simplified electrochemical cell models such as that presented in [26, 27] are not amenable for use in system-level planning study of BESS.

In view of the shortcomings identified in the cited references, the aim of this article is to report the development of a numerical approach to determine the minimum-cost Li-ion BESS design of a dispatchable RE-BESS power plant. The approach is to be used in the planning study stage of a Li-ion BESS, through utilizing the historical data of the renewable power resource. The approach adapts the physics-based Li-ion battery model derived in [28]. It takes into consideration the two major causes of the degradation of Li-ion cell: that of the resistive film growth at the cell solid-electrolyte interphase (SEI) which reduces the BESS power flow handling capability, and the consumption of active materials in the electrodes which decreases the BESS energy storage capacity [24]. Hence the degradation will impact the determination of the BESS capacity

and operational strategy. Furthermore, this investigation also considers the penalty cost imposed on the RE-BESS power plant for those instances when the plant is unable to meet the dispatch commitments. The design task is then formulated as a nonlinear optimization problem for which a modified particle swarm optimization (PSO) technique is used to obtain the least-cost solution. To the best knowledge of the authors, this is the first reported work which uses a dynamic degradation model of Li-ion BESS in a systematic BESS design study, and in the context of realizing a dispatchable RE-BESS power plant.

Accordingly, the remaining part of this manuscript is structured as follows: Section 2 provides the preliminary information essential for the development of the new degradation-conscious BESS model of the RE-BESS power plant described therein. Section 3 presents a method to design the operational power flow control strategy and analyzes the relationship between the strategy and the BESS capacity and state of energy control gain setting which are to be determined. Section 4 proposes a computational procedure to determine the optimal BESS design. Illustrative examples are given in Section 5, with main findings and conclusions shown in Section 6.

2. Development of Renewable Energy-Battery Energy Storage System Power Flow Model

2.1 System description and power dispatch market rules

While recognizing there are merits/demerits in each of the various possible configurations in integrating a BESS into a RE power plant, the schematic of Fig. 1 is adequate to relate the power flow relationship between the main components within the plant. In the figure, the renewable energy generator (REG) is an aggregation of WTG and/or PV panels and its associated power converters. The BESS, consisting of battery banks and converters, is inter-connected to the REG such that

$$\bar{P}_g(t) = \bar{P}_d(t)/\eta_d + \bar{P}_b(t)/\eta_b \qquad (1)$$

where $\bar{P}_g$ is the generated power from the REG, $\bar{P}_b$ is the power flow at the battery banks' terminals, and $\bar{P}_d$ is the power delivered to the grid. In this study, the time index t is expressed in hours, and the power quantities with the overbars are in per-unit on the RE plant rating P_N (in MW) base. η_b and η_d are the power conversion gains of the respective network components. While $\bar{P}_g$ is always positive, $\bar{P}_b$ is a bi-directional flow. When $\bar{P}_b < 0$, it indicates the discharging of the BESS and η_b equals to the reciprocal of the efficiency of the BESS converters. In this work, it is assumed $\bar{P}_d \geq 0$: the possibility of using the external grid to charge the BESS is not considered. For the ease of analysis, η_b and η_d are assumed constant.

As explained in the Introduction section, the role of the BESS is to ensure the dispatchability of the net RE-BESS plant output power $\bar{P}_d$. The design of the short-term dispatch strategy of $\bar{P}_d$ depends on the objectives and the prevailing power market regulatory conditions under which the power plant operates in. Usually under modern power market rules, all participating generating units must submit their generation schedules to the transmission system operator (TSO) in advance. In this study, it is assumed the RE plant participates likewise in such a scheme. The schedules $\bar{P}_{d,\mathrm{sch}}$ submitted by the RE-BESS plant operator would be specified at constant dispatch intervals (DIs), with each such intervals denoted herewith as τ hours, and y hours ahead. Typically, τ and y have the values of 1 and 24 respectively. However, the RE plant is allowed to submit new set of schedules, provided the new schedules are for periods which are not less than z hour(s) ahead. A typical value for z is 2. Any mismatch in the scheduled and the actual delivered powers would incur financial penalty on the RE plant operator. Such a penalty will also be considered in the present investigation.

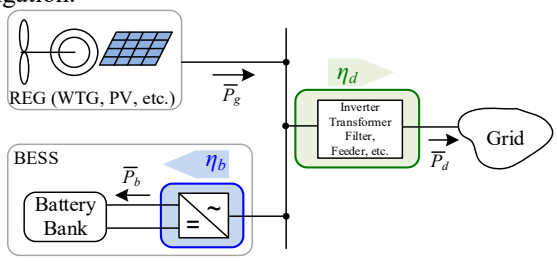

Fig. 1. General aggregate conceptual representation of a renewable energy-BESS power plant inter-connected to the external grid system. The arrows indicate the reference directions of the power flows.

2.2 An overview of a physics-based Li-ion battery cell model

Unlike the approaches used in existing works which utilized empirically-derived BESS models, the present investigation shall begin with a physics-based equivalent circuit model (ECM) of the Li-ion battery cell derived and validated in the authors' previous publication [28]. This model, as shown in Fig. 2, has been obtained from the well-established single particle model (SPM) of Li-ion battery cell, and by taking advantage of the fact that grid-connected BESS tends to operate under low C-rate [29]. Furthermore, the temperature of the BESS is maintained at a suitable level. For the problem in hand in which the BESS is expected to be housed within an environmentally-controlled facility, this would be a reasonable assumption [29].

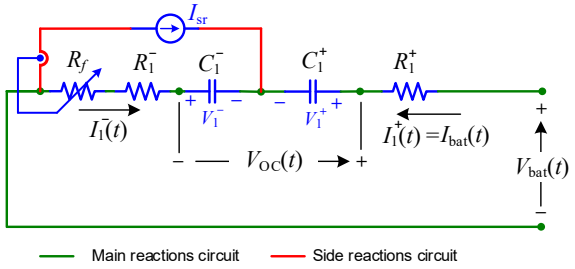

Fig. 2. The physics-based equivalent circuit of Li-ion battery cell derived from the isothermal single particle model [28]. The side-reactions current I_{sr} is always in the negative direction, with the result that it increases irreversibly the amount of the stored electric charges in the capacitor C_1^-.

The physics-based ECM shown in Fig. 2 contains a main reactions circuit which describes the charging/discharging process (i.e. intercalation/deintercalation), and a side reactions circuit which accounts for the battery degradation over the long term. In Fig. 2, I_{bat} is the applied cell current and V_{bat} is the cell terminal voltage. The relevant quantities of the main and the side reactions are identified with subscripts "1" and "sr" respectively. The two capacitors C_1^+ and C_1^- analogize the bulk storage of the lithium ions in the positive and negative electrodes respectively due to the main reactions. Capacitor voltages V_1^+ and V_1^- represent the open-circuit potentials

(OCPs) of the corresponding electrode, while $V_{\mathrm{OC}} = V_1^+ - V_1^-$ is the open-circuit voltage (OCV) of the battery cell. Resistances R_1^+ and R_1^- represent the resistive and charge transfer effects due to various internal processes.

The impact of the side reactions is studied through the inclusion of the side reactions current I_{sr} and the SEI resistance R_f, as shown in Fig. 2. The side reactions culminate in the growth of the SEI film in the negative electrode, and it results in capacity fade due to the loss of cyclable lithium species. The details of the explanation are provided in [28]. A recapitulation of the ECM and an explanation of the capacity fade is included in Appendix A, in order to facilitate the development of a system-level model of the BESS in the next sub-section. In essence, due to the presence of I_{sr}, the changes in the amounts of the electric charges Q_1^+ and Q_1^- in the two capacitors C_1^+ and C_1^- would not be the same. The relationship between the reduced ampere-hour (Ah) capacity Q_{loss} is given by

$$Q_{\mathrm{loss}}(t) = Q_1^+(t) + Q_1^-(t) - Q_{\mathrm{max}\,0} \geq 0 \tag{2}$$

where Q_{max0} is the Ah capacity at the beginning-of-life (BOL) of the battery when it is in the pristine state. Hereafter, the subscript "0" is attached to the respective cell variable when the battery is at the BOL.

2.3 Li-ion BESS power flow model for system-level studies

The physics-based ECM presented in the previous sub-section cannot be utilized directly in system-level studies of dispatchable power plants for two reasons. Firstly, important variables normally encountered in such studies include the BESS state of energy (SOE) [30], state of health (SOH) [8], stored energy E_1 [14, 28, 31], energy capacity E_{max} [7], amongst other quantities. These quantities have not been explicitly quantified in the ECM. So there is a need to establish the analytical relationships between the ECM circuit variables with the SOE, SOH, E_1 and E_{max}.

Secondly, the input variable of the BESS model has to be the power flow $\bar{P}_b$ at the BESS terminal as presented in (1), rather than the cell current I_{bat} as shown in the ECM. The relationship between $\bar{P}_b$ and I_{bat} can be established by assuming that all the battery cells in the BESS are identical, so that the cell power P_{bat} can be scaled up and normalized using a scaling factor λ, i.e.

$$\bar{P}_b(t) = \lambda P_{\mathrm{bat}} = \frac{N_{\mathrm{cell}}}{P_N} V_{\mathrm{bat}} I_{\mathrm{bat}} \tag{3}$$

where N_{cell} denotes the number of battery cells in the BESS. If the ECM is to be incorporated in system-level studies by making use of the algebraic relationship (3), an iterative numerical approach has to be used to solve the resulting set of differential algebraic equations which in turn leads to higher computational burden. Since the BESS model is intended for use in power system studies which would usually involve the examination of various grid system scenarios, the increase in solution time would be undesirable.

To address the above-mentioned difficulties, a physics-based system-level Li-ion BESS model is thus proposed next.

1) Reformulation of the state-space equation of the cell

Following the procedure presented in Appendix B, the physics-based ECM can be reformulated to yield:

$$\dot{E}_1 = P_1 = \eta_1(E_1, Q_{\mathrm{loss}}, P_{\mathrm{bat}}) \times P_{\mathrm{bat}} \tag{4a}$$

$$\dot{Q}_{\mathrm{loss}} = -I_{\mathrm{sr}}(E_1, Q_{\mathrm{loss}}, P_{\mathrm{bat}}) \tag{4b}$$

This new state-space battery cell model describes explicitly the amounts of the stored energy E_1 (defined in (B.1)) and of the side reactions-induced loss Q_{loss} of electric charges in the cell. The new input variable is the battery terminal power P_{bat}, as is required in power system-level studies. Also as shown in the appendix, the parameter η_1 is defined as the ratio between the total power of the capacitors C_1^+ and C_1^-, and P_{bat}. Such a model provides insightful information from which several battery performance indices can be derived, as follows.

2) Energy capacity, state of energy and state of health

The battery cell energy capacity E_{max} at any given time can be defined as the difference in the amounts of stored energy on capacitors C_1^+ and C_1^- when the battery operates from the end-of-discharge (EOD) state to the end-of-charge (EOC) state (or vice versa), i.e.

$$E_{\mathrm{max}}(Q_{\mathrm{loss}}) = \int_{Q_{\mathrm{EOD}}^+}^{Q_{\mathrm{EOC}}^+} V_1^+(Q_1^+)\,dQ_1^+ - \int_{Q_{\mathrm{EOD}}^-}^{Q_{\mathrm{EOC}}^-} V_1^-(Q_1^-)\,dQ_1^- \tag{4c}$$

Defined this way, E_{max} is the maximum amount of energy that can feasibly be stored in the cell. As when in deriving (B.1), due consideration is taken that $Q_{\mathrm{EOD}}^{\pm}$ and $Q_{\mathrm{EOC}}^{\pm}$ are functions of Q_{loss}. Thus E_{max} is also solely a function of Q_{loss}. E_{max} equals to the shaded area under the V_{OC} vs. Q_1^+ curve between Q_{EOD}^+ and Q_{EOC}^+, as shown in Fig. A1(a) for a given Q_{loss}. When the battery cell is at its BOL, by substituting $Q_{\mathrm{EOD}}^+ = Q_{\mathrm{EOC}}^- = 0$ and $Q_{\mathrm{EOD}}^- = Q_{\mathrm{EOC}}^+ = Q_{\mathrm{max0}}$ into (4c), one obtains the energy capacity E_{max0} of the battery cell at the BOL.

The SOE of the battery cell is defined herewith as the ratio of the stored energy E_1 to the energy capacity E_{max}, i.e.

$$\mathrm{SOE} = E_1(t) / E_{\mathrm{max}} \tag{4d}$$

Clearly at any degradation state of the battery, $0 \leq \mathrm{SOE} \leq 1$. SOE is therefore a measure of the state of the stored energy in the battery at any given time.

Next, a common practice in defining the cell lifetime is adopted: once the energy capacity E_{max} reaches ζ times of the initial capacity E_{max0}, the cell is considered to have reached its end of life (EOL). Typically ζ is 0.6−0.8 [32]. Hence, it can be readily shown that the SOH of the battery is given as

$$\mathrm{SOH} = \frac{1}{1-\zeta}\left(\frac{E_{\mathrm{max}}}{E_{\mathrm{max0}}} - \zeta\right) \tag{4e}$$

With (4e), SOH = 1 when the battery cell is at BOL, and SOH = 0 when it reaches the EOL state. The time for the cell to reach the EOL state from the BOL state is defined in this work as the lifetime T_{EOL} of the cell.

In view of (3), one can express the battery cell power in terms of the BESS terminal power $\bar{P}_b$ as

$$P_{\text{bat}} = \frac{1}{\lambda}\bar{P}_b(t) = \frac{E_{\max 0}}{\bar{E}_{b0}}\bar{P}_b(t) \tag{4f}$$

where $\bar{E}_{b0} = (N_{\text{cell}}/P_N)E_{\max 0}$ is the normalized BESS energy capacity at BOL on P_N MWh base.

Equations (4a) − (4f) allow a new power flow model (PFM) of the Li-ion BESS to be constructed.

3) Discussion on the physics-based power flow model

Fig. 3 shows the block diagram of the developed physics-based PFM. The model has at its input the BESS terminal power $\bar{P}_b$, with SOE, SOH, and $E_{\max}$ serve as the output variables. Furthermore, the model requires three look-up tables to determine η_1, I_{sr}, and $E_{\max}$, respectively, based on the cell terminal power P_{bat} and the two state variables E_1 and Q_{loss}. A graphical visualization of the relationships between η_1 and I_{sr} with E_1 and P_{bat} is shown in Fig. 4, which pertains to a 3.3-Ah lithium nickel manganese cobalt oxide ($LiNiMnCoO_2$ or NMC) battery. From Fig. 4(a), it can be seen that at BOL, SOH = 1 and the η_1 surface is relatively flat and close to the $\eta_1 = 1$ plane because of the low value of the resistance R_{eq}. The increase in the value of R_{eq}, due to the cell degradation, results in the decrease of SOH and an increase in the internal losses in the battery. This is reflected in the lowering of η_1 value during charging and in the rising of η_1 value during discharging. From SOH = 1 to SOH < 1, the amount of stored energy E_1 in the BESS relative to that at BOL reduces from 100% to some 50% in this example.

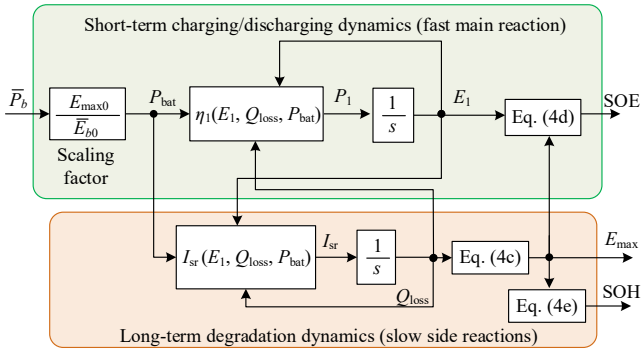

Fig. 3. Block diagram of the reformulated second-order Li-ion BESS power flow model for power system-level studies. BESS terminal power $\bar{P}_b$ is the input variable, whereas the stored energy E_1 and the loss capacity Q_{loss} are the two state variables. SOE, SOH, and $E_{\max}$ serve as the output variables which can be used for the strategization of the BESS operations.

Interestingly and as shown in Fig. 4(b), as the battery degrades, i.e., SOH < 1, the evolution of I_{sr} is such that in general, the magnitude of I_{sr} reduces. In view of (4b), this would indicate a decrease in the rate of capacity fade over time. This observation is consistent with the finding reported in [24, 33]. In the developed PFM, the rate of degradation, as reflected by (4b), is much lower compared to the rate of change of the stored energy E_1, as described by (4a). This can be seen from Fig. 4(b) that I_{sr} tends to be very low in comparison to $Q_{\max 0}$, the battery rated charge capacity. So when designing the short-term operational dispatch strategy in Section 3, one does not need to take into account the change in Q_{loss}, i.e., Q_{loss} can be assumed to be constant over the short term. However, as the side reactions current flow is persistent and continuous, the change in Q_{loss} can be appreciable over the lifetime of the BESS. So for study involving the long term behavior of the BESS, as in Section 4, the change in Q_{loss} has to be taken into consideration as the change will in turn impact on $E_{\max}$, η_1 as well as I_{sr}.

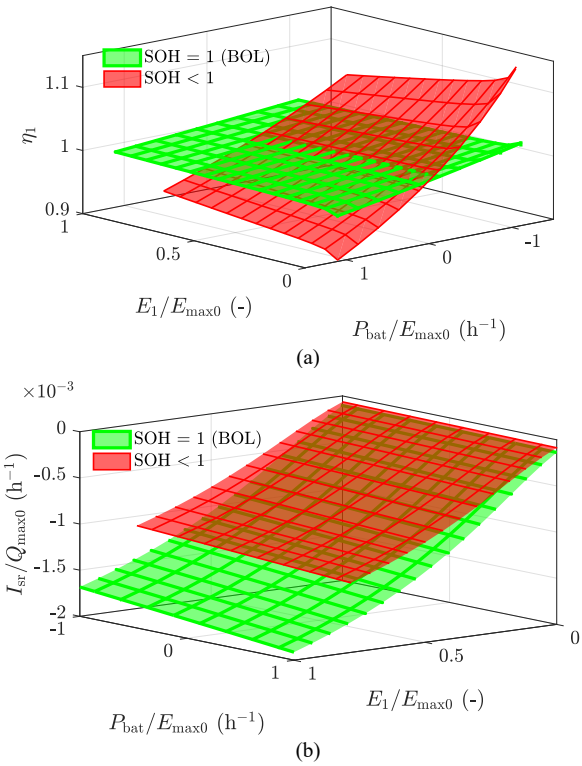

Fig. 4. Profiles of (a) η_1 and (b) I_{sr}, as functions of P_{bat} and E_1 when battery cell is at the BOL state (SOH = 1) and at the degradation state corresponding to $Q_{\text{loss}} = 0.5Q_{\max}$ (SOH < 1). P_{bat} and E_1 are normalized to the BOL energy capacity $E_{\max 0}$, and I_{sr} is normalized to the BOL charge capacity $Q_{\max 0}$.

3. Design of Battery Energy Storage System Control

As was explained in the Introduction section, the objective of this study is to determine the minimum-cost BESS energy storage capacity and power rating. In determining these parameters, however, one would need to take into account the BESS operational strategy. In the next sub-section, a binary mode BESS control scheme will be described. This control scheme is necessary in order to prevent the possible over-charge/over-discharge of the BESS due to the uncertain renewable input power. Accordingly, the dispatch reference signal will have to be modified and a method to do so is also shown in Sub-section 3.1. Furthermore, analysis of the resulting new RE-BESS dispatch control scheme shows the stability of the dispatch process will be guaranteed through the appropriate design of the BESS SOE controller.

In this section, the BESS capacity is assumed known *a priori*. Subsequently, an approach to determine the minimum-cost BESS energy storage capacity and power rating shall be described in Section 4.

3.1 A binary mode control scheme

Based on the PFM of the BESS derived in Sub-section 2.3 and the power dispatch market rules, Fig. 5 shows the schematic

of how the committed dispatch signal of $\bar{P}_d$ of the RE-BESS power plant is to be generated.

According to Fig. 5, the dispatch signal of $\bar{P}_d(t)$ is set as

$$\bar{P}_d(t) = \beta(t)\bar{P}_{d,\text{sch}}(t) + (1-\beta(t))\eta_d \bar{P}_g(t) \tag{5}$$

The binary mode coefficient β is used to determine which one of the following two operating modes the BESS shall be in.

Normal operating mode $\beta = 1$: Under this mode, the dispatch schedule $\bar{P}_{d,\text{sch}}$ is deemed achievable and the delivered power signal $\bar{P}_d = \bar{P}_{d,\text{sch}}$. $\bar{P}_d$ is to consist of two parts: $\bar{P}_{d,\text{ref}}$ and $\bar{P}_{d,\text{adj}}$. First and as shown in Fig. 5, $\bar{P}_{d,\text{ref}}$ is the predetermined schedule of the dispatch in the DI τ calculated based on the forecasted wind speed/solar irradiance and prevailing market rules, among other factors. As various techniques have been reported in the literature on such pre-scheduling [12, 13, 18-22], it is not the intent of the present work to develop yet another pre-scheduling technique. Suffice to say that the determination of $\bar{P}_{d,\text{ref}}$ shall consider the limited energy storage capacity of the BESS, so the BESS SOE is bounded. This is to prevent the over-charge or over-discharge of the battery, as this can lead to accelerated aging or permanent damage of the BESS. If the forecast $\bar{P}_{g,f}$ on $\bar{P}_g$ is perfectly accurate and the subsequent charging or discharging action of the BESS is such that the SOE is within bounds, then $\bar{P}_d = \bar{P}_{d,\text{ref}} = \bar{P}_{d,\text{sch}}$. Unfortunately, due to the inevitable forecast error, the SOE may exceed the bound [0, 1]. Fortunately, the power market rules described earlier allow revised $\bar{P}_{d,\text{sch}}$ to be submitted z hours before the power delivery. So a possible strategy would be to modify those $\bar{P}_{d,\text{sch}}$ in DIs which are z hours ahead and beyond, by introducing an adjustment term $\bar{P}_{d,\text{adj}}$ to these $\bar{P}_{d,\text{ref}}$, i.e.

$$\bar{P}_{d,\text{sch}}(t) = \bar{P}_{d,\text{ref}}(t) + \bar{P}_{d,\text{adj}}(t) \tag{6}$$

$\bar{P}_{d,\text{adj}}$ has to be constant too within each DI. In Fig. 5, $\bar{P}_{d,\text{adj}}$ is shown generated from the SOE produced by the PFM, i.e., Fig. 3. Details of the control scheme to yield $\bar{P}_{d,\text{adj}}$ shall be given in the next sub-section.

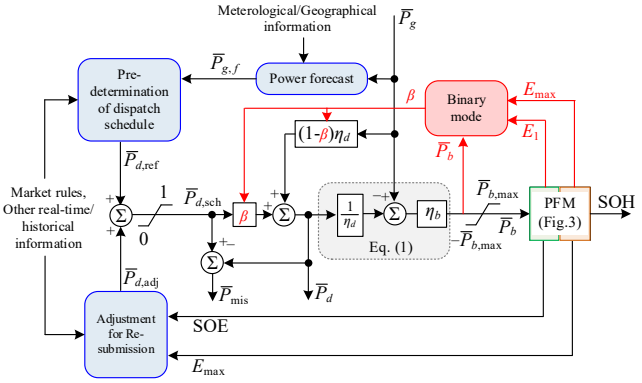

Fig. 5. Schematic of the BESS control system showing how the RE-BESS dispatch signal $\bar{P}_d$ is generated from the forecast $\bar{P}_{g,f}$. The binary coefficient β is used to switch between the operating modes determined by (8).

Also shown in Fig. 5 is the limit placed on $\bar{P}_{d,\text{sch}}$ due to the RE plant power rating P_N (1 p.u.):

$$0 \le \bar{P}_{d,\text{sch}}(t) \le 1 \tag{7a}$$

Furthermore, as the power capacity of a typical Li-ion BESS is usually higher than the requirement of most grid applications, it is assumed that the BESS power $\bar{P}_b$ is limited by the rating $\pm\bar{P}_{b,\max}$ (in p.u. on plant rating base P_N) of the power converters [34, 35]:

$$-\bar{P}_{b,\max} \le \bar{P}_b(t) \le \bar{P}_{b,\max} \tag{7b}$$

As an illustration, consider the example of Fig. 6. Over the intervals $t < t_a$, $t_b < t < t_c$, and $t > t_d$, SOE is predicted to be within the bounds [0, 1]. So over these periods, $\bar{P}_d = \bar{P}_{d,\text{sch}}$, i.e., $\beta = 1$.

Floating operating mode $\beta = 0$: due to the inaccuracies in the wind/solar power forecast and in order to deliver the committed dispatch $\bar{P}_{d,\text{sch}}$, a situation may arise when the BESS is called upon to either absorb or generate power but is unable to do so because the BESS is already fully-charged or fully-discharged. So in this mode, the RE-BESS is to deliver all the power the REG is generating, i.e. $\bar{P}_d = \eta_d \bar{P}_g$, rather than delivering the committed dispatch $\bar{P}_{d,\text{sch}}$. In this mode, $\bar{P}_b$ is zero and the SOE remains at its maximum (1 p.u.) or minimum (0) levels. Using the example of Fig. 6 again, over the period $t_a < t < t_b$, SOE = 1 p.u., which means the battery is fully-charged. Conversely over the period $t_c < t < t_d$, SOE = 0 and the BESS is fully-discharged. Over these periods, $\bar{P}_{d,\text{sch}}$ cannot be met and the RE-BESS power plant is to dispatch all the power generated by the REG.

The instance at which the switch-over between the two modes is determined based on the forecasted SOE: SOE_f. SOE_f is evaluated from the forecast $\bar{P}_{g,f}$ whereby $\bar{P}_b = \bar{P}_{g,f} - \bar{P}_{d,\text{sch}}$, and E_1 is calculated using (4a), (4d) and (4f):

$$\text{SOE}_f(t) = \frac{E_1(t-\Delta t)}{E_{\max}} + \frac{E_{\max 0}}{E_{\max}\bar{E}_{b0}} \int_{t-\Delta t}^{t} \eta_1(t')\bar{P}_b(t')dt' \tag{8a}$$

Δt is a pre-specified time step, and β can then be determined:

$$\beta(t) = \begin{cases} 1, & \text{SOE}_f(t) \in [0,\ 1] \\ 0, & \text{otherwise} \end{cases} \tag{8b}$$

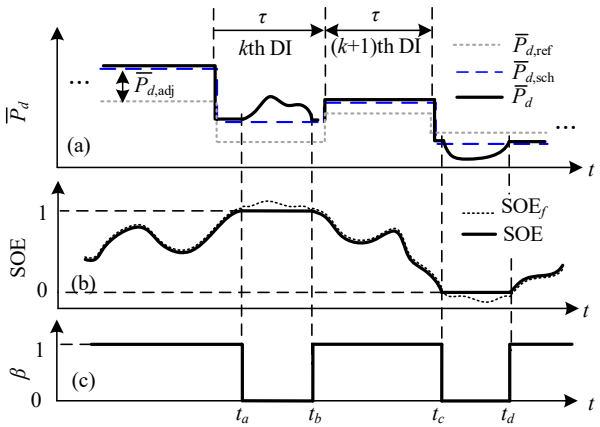

Fig. 6. Illustration of the profiles of (a) dispatched power reference $\bar{P}_{d,\text{ref}}$, scheduled power $\bar{P}_{d,\text{sch}}$ and the amount of the associated adjustments $\bar{P}_{d,\text{adj}}$ (b) forecasted state of energy SOE_f and SOE; (c) binary mode coefficient β.

3.2 *Determination of* $\bar{P}_{d,adj}$

In this sub-section, the particular dispatch control strategy proposed in [36] will be used to demonstrate how the

adjustment term $\bar{P}_{d,\text{adj}}$ is to be generated based on SOE$_f$. First, assume the error e_f in the forecast $\bar{P}_{g,f}$ of the REG power is normally distributed and has zero mean such that

$$\bar{P}_{g,f}(t) = \bar{P}_g(t) + e_f(t) \tag{9}$$

Next, set the reference of the dispatch power $\bar{P}_{d,\text{ref}}$ for the k-th DI as the average of the forecasted power $\bar{P}_{g,f}$ within the DI,

$$\bar{P}_{d,\text{ref}}(t) = \frac{1}{\tau}\int_{t_k}^{t_{k+1}} \eta_d \bar{P}_{g,f}(t')dt' \tag{10}$$

t_k and $t_{k+1} = t_k + \tau$ denote the beginning and the end times of the k-th DI, respectively.

Since the forecast error e_f has zero mean, the calculated battery power $\bar{P}_b$ will only consist of the oscillating components of $\bar{P}_{g,f}$ and it shall have zero mean. As explained in Appendix B, η_1 is a nonlinear function of E_1, P_{bat} and Q_{loss} of the Li-ion battery cell. So the power flow P_1 in the capacitors C_1^+ and C_1^- will not have zero mean value even as the mean value of $\bar{P}_b$ (i.e. P_{bat}) is zero. To calculate SOE based on P_1 and (4d), as shown in Fig. 3, will result in a steady downward drift in the SOE. This will lead to the BESS being over-discharged. In order to prevent this from happening, it is proposed the adjustment $\bar{P}_{d,\text{adj}}$ is to be set proportional to the difference between SOE and its set-point value SOE*. K_c is to denote the proportionality gain. Furthermore, as explained in Sub-section 2.1 on power market rules, for the k-th DI, the constant adjustment $\bar{P}_{d,\text{adj}}$ has already been committed at least z hour(s) ahead. And as $\bar{P}_{d,\text{adj}}$ can only be updated every τ-hour, so the estimated SOE$_f$ is to be sampled and held for τ hour(s). Mathematically, it means that

$$\bar{P}_{d,\text{adj}}(t) = K_c[\text{SOE}^* - \text{SOE}(t_k - z)] \quad t \in [t_k, t_{k+1}] \tag{11}$$

In using the strategy (11), SOE* can be specified based on the design objective. For example, SOE* shall be set to a relatively low value so as to increase the lifetime of the particular type of Li-ion battery considered in [36]. On the other hand, SOE* can be set corresponding to a mid-level, e.g., SOE* = 0.5, so as to allow the BESS almost equal charging and discharging capabilities. It is this latter philosophy the present work has adopted, although the presented scheme does allow the adjustment of SOE* to suit the type of Li-ion battery cell used.

In Fig. 6, an example of $\bar{P}_{d,\text{adj}}$ has been added to illustrate the above proposed adjustment principle.

3.3 Adaptive tuning of K_c for long term BESS operations

The gain setting K_c will affect the dynamic performance of the dispatch control scheme and in this sub-section, the determination of suitable ranges for the parametric value of K_c shall be demonstrated.

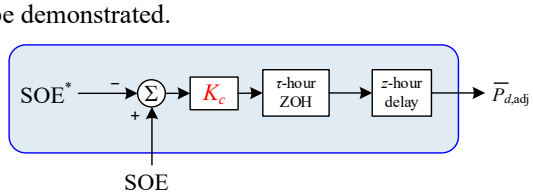

Fig. 7. Block diagram of the proposed SOE controller $G_c(s)$ obtained when implementing the strategy (11) which in turn lead to a closed-loop BESS control system shown on Fig. 5.

The operation to generate $\bar{P}_{d,\text{adj}}$ based on (11) is shown in Fig. 7 in which the τ-hour zero-order hold (ZOH) and the z-hour delay blocks have been incorporated. The small-signal transfer function $G_c(s)$ of the control block is

$$G_c(s) = \frac{\Delta\bar{P}_{d,\text{adj}}(s)}{\Delta\text{SOE}(s)} \approx K_c \frac{1 - e^{-\tau s}}{\tau s} e^{-zs} \tag{12}$$

Next, using (4a) and (4d), and since $P_{\text{bat}} = (E_{\text{max0}}/\bar{E}_{b0})\bar{P}_b$, the comparatively fast main reactions dynamics in the PFM of Fig. 3 can be expressed as the transfer function $G_b(s)$:

$$G_b(s) = \frac{\Delta\text{SOE}(s)}{\Delta\bar{P}_b(s)} \approx \frac{\eta_1}{\bar{E}_{b0}} \frac{E_{\text{max0}}}{E_{\text{max}}} \frac{1}{s} = \frac{K_b}{s} \tag{13}$$

where $K_b = \eta_1(E_{\text{max0}}/E_{\text{max}})/\bar{E}_{b0}$. In obtaining (13), the following assumptions are made. First, as explained in Section 2.3, Q_{loss} would be relatively constant over short intervals. So E_{max} is assumed constant over the DI. Next as shown in Fig. 4(a), although η_1 would be a function of SOE and P_{bat}, however, for low C-rate application as in grid systems, $P_{\text{bat}}/E_{\text{max0}}$ would be very low and hence, $\eta_1 \approx 1$. Therefore, K_b in (13) can be considered constant for the short-term dispatch study.

The ZOH and delay blocks introduce nonlinearities into the system. In general, a closed-loop control system containing ZOH and delay actions can lead to system instability if it is not properly designed [37, 38]. The stability issue of the dynamical system (12) and (13) can be studied by examining the transfer function (14) which governs the dispatch control process through regulating the BESS SOE about SOE*:

$$\begin{aligned}\frac{\Delta\text{SOE}(s)}{\Delta\text{SOE}^*(s)} &= \frac{G_c(s)G_b(s)}{1 + G_c(s)G_b(s)} \\ &\approx \frac{2K_dK_b(-zs+2)}{\tau z s^3 + 2(\tau+z)s^2 + 2(2 - K_dK_b z)s + 4K_dK_b}\end{aligned} \tag{14}$$

In deriving (14), the transcendent transfer function shown as (12) has been approximated using the first-order Padé function

$$e^{-bs} \approx \frac{-bs+2}{bs+2} \tag{15}$$

Applying the Routh-Hurwitz criterion to (14) yields the following ranges for K_c in order to guarantee the stability of the dispatch control process:

$$0 < K_c < K_{c,\text{UL}} = \frac{2(\tau+z)}{K_b(2\tau+z)z} \tag{16}$$

Naturally the estimation on the upper limit $K_{c,\text{UL}}$ could be improved if higher-order Padé approximation is used for the ZOH and delay blocks. Nevertheless, the first-order Padé approximation adopted here should be sufficient to demonstrate an important dispatch strategy design principle: (16) shows that the power dispatch scheme as depicted on Fig. 5 and Fig. 7 can be unstable if the BESS control setting K_c is designed without considering the stipulated market rules on τ and z, and the BESS characteristics gain K_b. This is an important finding which has yet to be reported in the literature pertaining to the design of BESS control scheme, and in the attempt to achieve of dispatchability of RE-BESS power plant.

Even with the application of (16), there still remains a range of setting values for K_c. Indeed, due to the presence of the battery internal resistance R_{eq}, a persistent downward trend has been observed in the SOE during the dispatch process when similar BESS control scheme has been considered [36]. This is obviously an undesirable outcome. This phenomenon can be demonstrated by considering a hypothetical RE-BESS power plant which is to provide hourly-constant dispatch to an external grid system using the proposed feedback control scheme. The results of simulation studies at different values of K_c are as shown in Fig. 8. It shows that a relatively low value on K_c setting will result in such a downward trend. While higher setting value on K_c would impose tighter SOE regulation and help to eliminate this downward trend, unfortunately, this would incur more drastic BESS charging and discharging actions. The SOE will impinge on its limits more frequently, with the result that the dispatch commitment may have to be forego in order to protect the BESS from permanent damages. However, as will be discussed in Section 4, foregoing the committed dispatch will incur penalty cost to the RE-BESS operator. Clearly a judicious choice of setting value for K_c is called for in order to ensure prudent BESS operations. A possible technique to do so is proposed, as follows.

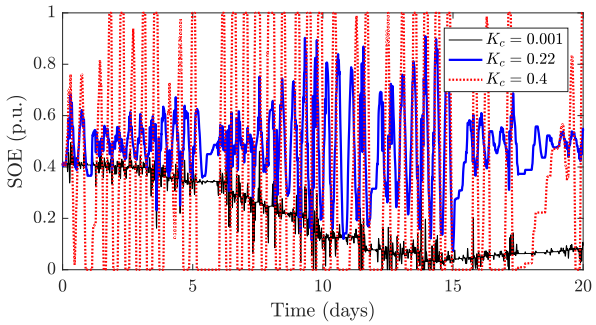

Fig. 8. Effect of K_c setting value on the SOE profile. Small K_c setting value can lead to persisting deviation of SOE from its reference value while large setting value of K_c can cause drastic fluctuations in SOE and even unstable dispatch process

Over the long term, the cell energy storage capacity E_{max} and η_1 will be reduced due to the side reactions. In order to ensure stable dispatch operations, (16) shows that the product K_cK_b must be less than $2(\tau+z)/(2\tau+z)z$, a constant. It is now proposed that K_cK_b is to be maintained at a constant value throughout the lifetime of the BESS. In (13), K_b is seen to be proportional to $1/E_{\text{max}}$, so K_c will be tuned to be proportional to E_{max}, as follows:

$$K_c(t) = K_{c0}E_{\text{max}} / E_{\text{max}\,0} \tag{17}$$

The last expression provides the following useful approach to the design of the BESS SOE controller: one can carry out a series of time-domain simulation study of the RE-BESS power plant based on historical wind or solar power and for a range of K_{c0} values. By tracking the value of E_{max} as the BESS operates and adaptively tuning K_c in accordance to (17), the long-term behavior of the BESS variables, including that of SOE and E_{max}, can be monitored for performance assessment. A suitable value for K_{c0} can then be determined so that during the normal BESS operating mode, the downward drift in SOE will be removed while stability of the dispatch system is guaranteed. An example of the outcome of such a SOE controller tuning approach is shown in Fig. 8 where with K_{c0} set at 0.22, the rather satisfactory SOE profile as represented by the blue curve was obtained.

4. Determination of Battery Energy Storage System Power and Energy Ratings

The next task is to extend the above numerical approach so that the BESS power rating and stored energy capacity can be determined, based on the proposed BESS control scheme described in the previous section. The power rating and energy capacity are determined by considering the capital cost of the BESS as well as the cost for failing to meet the dispatch power commitment.

4.1 Annualized life cycle cost of the battery energy storage system

The capital cost of the BESS can be considered as a function of the power rating $\bar{P}_{b,\text{max}}$ of the associated power converter, and the battery bank stored energy capacity $\bar{E}_{b0}$. In this article, the capital cost (TC) of the BESS is expressed as

$$\text{TC} = (k_1\bar{P}_{b,\text{max}} + k_2\bar{E}_{b0}) \times P_N \tag{18}$$

where k_1 and k_2 are the BESS cost per MW and cost per MWh. Their values are obtainable from the manufacturers or the literature.

Let i be the interest rate and T_{RE} denotes the specified service lifespan of the RE-BESS. Then the annualized cost (AC) of the BESS can be calculated from the capital recovery factor (CRF), i.e.

$$\text{CRF} = \frac{i(1+i)^{T_{\text{RE}}}}{(1+i)^{T_{\text{RE}}} - 1} \tag{19}$$

$$\text{AC} = \text{TC} \times \text{CRF} \tag{20}$$

The annualized replacement cost (AR) of the BESS is

$$\text{AR} = (k_2\bar{E}_{b0}P_N) \times \sum_{m=1}^{N}(1+i)^{-mT_{\text{EOL}}} \times \text{CRF} \tag{21}$$

where N is the number of times the BESS will need replacement over the lifespan of the RE-BESS plant. As defined in Sub-section 2.3, T_{EOL} is the lifetime of the BESS, and as will be demonstrated in Sub-section 5.1, T_{EOL} can be predicted via the time-domain simulation using the PFM (Fig. 3) and applying the control strategy proposed in Section 3. N is the next higher integer greater than or equal to $T_{\text{RE}}/T_{\text{EOL}}$.

4.2 Cost of failing to meet dispatch obligations

As explained in Sub-section 3.1, there will be instances when the actual delivered power $\bar{P}_d$ differs from the committed schedule power $\bar{P}_{d,\text{sch}}$ during the BESS *floating mode* (β = 0) operations. The amount of the mismatched energy, and/or the mismatched power if the specific market rule applies, will be used to calculate the financial penalty imposed by the TSO on the RE-BESS operator. The mismatched power $\bar{P}_{\text{mis}}$ is defined as

$$\bar{P}_{\text{mis}}(t) = \bar{P}_{d,\text{sch}}(t) - \bar{P}_d(t) \tag{22}$$

The amount of the mismatched energy $\bar{E}_{\text{mis}}$ of the k-th DI ($t_k \le t \le t_{k+1}$) is

$$\bar{E}_{\text{mis},k} = \int_{t_k}^{t_{k+1}} |\bar{P}_{\text{mis}}(t')|\, dt' \tag{23}$$

In the present study, the amount of the mismatched energy will be used to calculate the financial penalty. Specifically, the three-tier mismatched energy penalty scheme reported in [14] is adopted wherein at the k-th DI, $\bar{E}_{d,k} = \bar{P}_{d,\text{sch}}(t_k) \times \tau$ is calculated. Then if $\bar{E}_{\text{mis},k}/\bar{E}_{d,k}$ is less than l%, $\bar{E}_{\text{mis},k}$ is deemed to be sufficiently low and is acceptable. It therefore attracts no penalty. The no-penalty energy level $\bar{E}_{0,k}$ is then set equal to $\bar{E}_{\text{mis},k}$. However, if $l\% \le \bar{E}_{\text{mis},k}/\bar{E}_{d,k} \le h\%$, $\bar{E}_{\text{mis},k}$ is sub-divided into the no-penalty level $\bar{E}_{0,k}$ and the lower-tier penalty level $\bar{E}_{l,k}$. $\bar{E}_{0,k}$ and $\bar{E}_{l,k}$ are calculated in accordance to the rules given in Table 1. Finally, if $\bar{E}_{\text{mis},k}/\bar{E}_{d,k} \ge h\%$, $\bar{E}_{\text{mis},k}$ is divided into the three portions $\bar{E}_{0,k}$, $\bar{E}_{l,k}$ and $\bar{E}_{h,k}$, which are evaluated in the manner given in Table 1.

Table 1
Calculation of the Mismatched Energy Components.

	$\bar{E}_{\text{mis},k}/\bar{E}_{d,k} < l\%$	$l\% \le \bar{E}_{\text{mis},k}/\bar{E}_{d,k} < h\%$	$\bar{E}_{\text{mis},k}/\bar{E}_{d,k} \ge h\%$
$\bar{E}_{0,k}$	$\bar{E}_{\text{mis},k}$	$\bar{E}_{d,k} \times l\%$	$\bar{E}_{d,k} \times l\%$
$\bar{E}_{l,k}$	0	$\bar{E}_{\text{mis},k} - \bar{E}_{d,k} \times l\%$	$\bar{E}_{d,k} \times (h-l)\%$
$\bar{E}_{h,k}$	0	0	$\bar{E}_{\text{mis},k} - \bar{E}_{d,k} \times h\%$

The total amount of the penalty cost PC incurred due to the mismatched dispatch over the lifetime of the BESS is

$$\text{PC} = \sum_{k=1}^{k_{\text{EOL}}} (C_{\text{IH}} \bar{E}_{h,k} + C_{\text{IL}} \bar{E}_{l,k}) \times P_N \tag{24}$$

where C_{IH} and C_{IL} denote the higher- and the lower-tier fix generation imbalance charge, respectively. $k_{\text{EOL}} = T_{\text{EOL}} \times 365 \times 24/\tau$ is the total number of DIs over the lifetime of the BESS.

Finally, the annualized penalty cost (AP) is

$$\text{AP} = \text{PC} \times \text{CRF}_B \tag{25}$$

where CRF_B is the capital recovery factor for the BESS, i.e.

$$\text{CRF}_B = \frac{i(1+i)^{T_{\text{EOL}}}}{(1+i)^{T_{\text{EOL}}} - 1} \tag{26}$$

4.3 Procedure to determine the minimum-cost BESS design

It is proposed that the determination of the optimum BESS power rating and energy storage capacity shall be based on the minimization of the overall annualized cost J, where

$$J = \text{AC} + \text{AR} + \text{AP} \tag{27}$$

According to (18)–(27), it can be seen that AC is determined by the converter power rating $\bar{P}_{b,\max}$ and the BESS energy capacity $\bar{E}_{b0}$ at BOL, AR is governed by $\bar{E}_{b0}$ and T_{EOL}, whereas AP is impacted by $\bar{E}_{\text{mis},k}$ and T_{EOL}. Amongst these parameters, $\bar{E}_{\text{mis},k}$ and T_{EOL} can only be obtained via time-domain simulation, and they are in turn affected by the selection of design parameters $\bar{P}_{b,\max}$, $\bar{E}_{b0}$ and control gain setting K_{c0}. So the numerical iterative procedure to search for the optimal combination of $\bar{P}_{b,\max}$, $\bar{E}_{b0}$ and K_{c0} involves calculating $\bar{P}_{d,\text{ref}}$ based on the forecast $\bar{P}_{g,f}$, and a set of initial values of $\bar{P}_{b,\max}$, $\bar{E}_{b0}$ and K_{c0}. A time-domain simulation is then carried out based on the PFM and the control scheme shown on Fig. 3, Fig. 5, and Fig. 7. Whence T_{EOL} and $\bar{E}_{\text{mis},k}$ are calculated, and J is then evaluated.

In this study, the search for the minimum J is accomplished using PSO technique. Specifically, to minimize J, the equality constraints consist of the power balance equation (1), BESS PFM equations (4a)–(4f), and the control strategy governs by (5), (6), (8), (11) and (17), while (7) and (16) are the inequality constraints for the optimization. The above procedure is repeated until the least cost solution is obtained.

PSO is a simple and effective metaheuristic optimization technique. The technique is initialized with some population of random candidates and a search algorithm to reach the global optimum for the defined objective function [39]. Mathematically for a D-dimensional optimization problem, the position vector $\mathbf{x} \in \mathbb{R}^D$ and velocity vector $\mathbf{v} \in \mathbb{R}^D$ of the i-th particle in the iteration number j are expressed as

$$\mathbf{x}_i^j = [x_{i,1}^j \quad x_{i,2}^j \quad \cdots \quad x_{i,D}^j] \tag{28a}$$

$$\mathbf{v}_i^j = [v_{i,1}^j \quad v_{i,2}^j \quad \cdots \quad v_{i,D}^j] \tag{28b}$$

Each position vector represents a potential solution to the problem, while the velocity vector indicates the extent of variation in the updating procedure. The equations with which the velocity and the positions of the particles are updated are

$$\mathbf{v}_i^{j+1} = w\mathbf{v}_i^j + c_1 r_{1,i}^j (\mathbf{p}_i^j - \mathbf{x}_i^j) + c_2 r_{2,i}^j (\mathbf{g}^j - \mathbf{x}_i^j) \tag{29a}$$

$$\mathbf{x}_i^{j+1} = \mathbf{x}_i^j + \mathbf{v}_i^{j+1} \tag{29b}$$

where $\mathbf{p}$ is the recorded best solution for specific particle and $\mathbf{g}$ is the global optimal solution among all $\mathbf{p}$. r_1 and r_2 are two random numbers between 0 and 1. w, c_1 and c_2 are referred as the inertia constant, cognitive scaling parameter, and social scaling parameter, respectively. These coefficients determine how much of each components from the previous iteration affect the next movement of the position vector.

For the problem in hand, the position vector is the 3-dimensional vector, i.e.

$$\mathbf{x}_i^j = [\bar{E}_{b0,i}^j \quad K_{c0,i}^j \quad \bar{P}_{b,\max,i}^j] \tag{30}$$

By substituting K_b in (13) into (16), one obtains

$$0 < K_{c0,i}^j < \frac{2(\tau+z)}{(2\tau+z)z} \frac{1}{\bar{E}_{b0,i}^j} \tag{31}$$

Hence it is clear that the lower bound on K_{c0} is 0 whereas the upper bound on K_{c0} is dependent of $\bar{E}_{b0}$. So instead of using fixed search boundary for each element of **x,** as is often the case when using the conventional PSO algorithm, the search algorithm is modified so that a dynamic boundary satisfying (31) is imposed. This is achieved by checking the stability condition (31) for each $K_{c0,i}^j$ and then set $K_{c0,i}^j$ in accordance to the following rule:

$$K_{c0,i}^{j}=\begin{cases} K_{c0,i}^{j}, & \text{if } K_{c0,i}^{j}\bar{E}_{b0,i}^{j}<\dfrac{2(\tau+z)}{(2\tau+z)z} \\ \dfrac{2(\tau+z)}{(2\tau+z)z}\dfrac{1}{\bar{E}_{b0,i}^{j}}, & \text{if } K_{c0,i}^{j}\bar{E}_{b0,i}^{j}\geq\dfrac{2(\tau+z)}{(2\tau+z)z} \end{cases} \quad (32)$$

With $K_{c0,i}^{j}$ set in accordance to (32), the stability of the dispatch control process will be assured.

5. Illustrative Examples

The purpose of this section is to firstly validate the developed PFM of the Li-ion BESS by comparing the results of simulation using this model with those obtained using other established Li-ion battery models, and secondly, to illustrate the proposed BESS design methodology. A hypothetical 100-MW wind farm (P_N = 100 MW) is assumed and in order to fairly evaluate the performance of the BESS due to degradation, the same one-year wind speed data obtained from [40] was used repeatedly over several consecutive years to construct the long-term wind power generation profile $\bar{P}_g$. Based on $\bar{P}_g$, the forecasted wind power $\bar{P}_{g,f}$ was then generated by assuming the error e_f in the forecast was normally distributed with zero mean, and has the standard deviation of 15%, a level typical in wind power forecast. Next, the hourly constant schedule $\bar{P}_{d,\text{ref}}$ was calculated using (9) and (10). The wind power data was sampled at 1-minute interval. With regard to the specific prevailing market rule assumed in this study, τ = 1, z = 2, l = 1.5, h = 7.5, C_{IH} = \$1000/MWh and C_{IL} = \$500/MWh. For the BESS, k_1 = \$100×10^3/MW, k_2 = \$200×10^3/MWh [14]. It is further assumed that T_{RE} = 20 years, i = 8.5%, for which CRF is 1.075 according to (19). The battery parameters are given in Table A.1 for a 3.3-Ah NMC cell with E_{max0} = 12.5 Wh. The EOL of the BESS is reached when ζ is 0.6.

5.1 Comparison with existing physics-based battery models

As was demonstrated in the authors' previous study [28], the laboratory results obtained in the standard constant-current constant-voltage (CCCV) cycling test reported in [24] were satisfactorily replicated by the physics-based ECM described by (A.1)–(A.8). Furthermore, simulation results based on the physic-based ECM were also found to be in excellent agreement with those obtained based on the electrochemical SPM of Li-ion cell as well as by the well-established pseudo-two-dimensional electrochemical model. Therefore the physics-based ECM and the electrochemical SPM are deemed sufficiently accurate to represent grid-connected Li-ion BESS.

Accordingly, in this sub-section, the accuracy and the computational burden of the developed PFM shown as Fig. 3 shall be compared against that of the physics-based ECM and the electrochemical SPM. In the present investigation, instead of using the CCCV test protocol, long-term simulation was conducted in MATLAB R2016a/Simulink 8.7 environment using the aforementioned dynamic multi-year wind power profiles.

The outcome of the comparison of the simulation results is summarized in Table 2 and a snapshot of the resulting waveforms is shown in Fig. 9. Fig. 9(a) and Fig. 9(b) show the comparison of the simulated power $\bar{P}_d$ delivered to the grid, SOE, and BESS power $\bar{P}_b$ over a particular 12-hour period in the 8$^{\text{th}}$ year of the dispatch operations. Expanded view of selected interval is provided on the right. It can be seen that the proposed PFM is able to accurately capture the major dynamic behaviors of the system. The expanded plots of Fig. 9(a)–Fig. 9(c) show the excellent agreement between the three models on the predicted occurrences of the dispatch mismatch due to the constraints placed on the SOE and $\bar{P}_b$. When compared against the results obtained using the SPM, the root-mean-square errors (RMSEs) of $\bar{P}_b$ and SOE computed using the developed PFM are less than 0.4%. The predicted capacity fade profile is shown in Fig. 9(d). The EOL predicted by SPM, physics-based ECM and the proposed PFM are 2773 days, 2755 days and 2751 days, respectively: the differences in the predicted lifetimes are less than 1%.

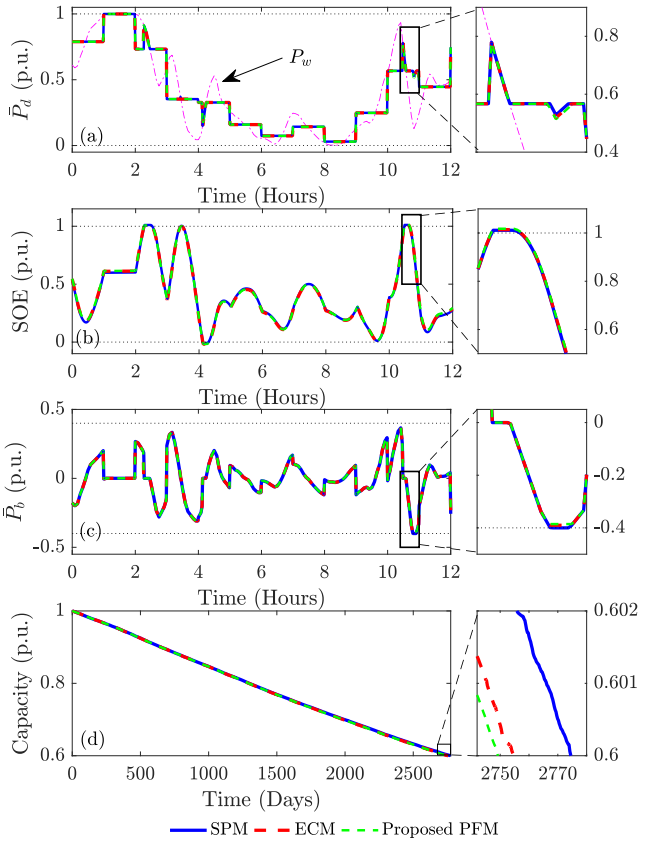

Fig. 9. Comparison of simulation results using the proposed PFM, a physics-based ECM and SPM: (a) Dispatched power; (b) SOE; (c) BESS power and (d) BESS stored energy capacity. The black dotted lines indicate the relevant operating limits of the RE-BESS. Expanded view of selected section is shown on the right. In this example, $\bar{P}_{b,\text{max}}$ = 0.4 p.u., $\bar{E}_{b0}$ = 0.42 p.u. K_{c0} = 0.012.

Table 2
Comparison of the performance of the electrochemical single particle model (SPM), the physics-based equivalent circuit model (ECM) and the developed power flow model (PFM) of the Li-ion BESS.

Model	Δt	RMSE (%)		T_{EOL} (days)	CPU Time (s)
		$\bar{P}_b$	SOE		
SPM	5 s	-	-	2773	32.3
Physics-based ECM	60 s	0.19	0.31	2755	2.5
Proposed PFM	60 s	0.23	0.34	2751	1.3

Furthermore, it can be seen from the last column of Table 2 that the physics-based ECM has, compared to the SPM, reduced the solution time by a factor of more than 10. This is due to the reduction in the order of the model and the removal of the computational steps required to convert the BESS power to battery current in the ECM [28]. Further reduction on the solution time by a factor of almost 2 is achieved when using the developed PFM. This is because for this dispatchable renewable generation application, the required variables for the dispatch control, i.e., SOE, $E_{\max}$ and SOH, are directly obtained in the form of the model states or outputs. As explained in Sub-section 2.3, such reduction in the solution time is most desirable, considering the proposed PFM is to be used in power system planning and design studies in which one can expect a large number of scenario is to be examined.

5.2 Optimum BESS design

In determining the optimum BESS design, the PSO algorithm was applied using $c_1 = c_2 = 2$. w and the particle number were selected to be 0.8 and 20 respectively.

Fig. 10 and Fig. 11 show the optimal solution was found after 16 iterations, yielding $\bar{E}_{b0}^{\text{opt}} = 0.226$ p.u. (22.6 MWh), $\bar{P}_{b,\max}^{\text{opt}} = 0.31$ p.u. (31 MW), and $K_{c0}^{\text{opt}} = 0.016$. The minimum overall annualized cost J is about $\$1.41\times10^6$, the corresponding AC, AR and AP are $\$0.81\times10^6$, $\$0.38\times10^6$, and $\$0.22\times10^6$, respectively.

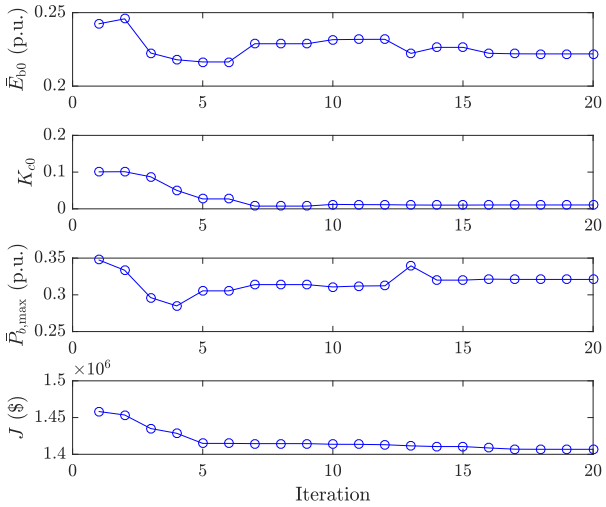

Fig. 10. Outcome of PSO search on (a) energy capacity of BESS; (b) feedback control gain; (c) power rating of BESS; (d) overall annualized cost J.

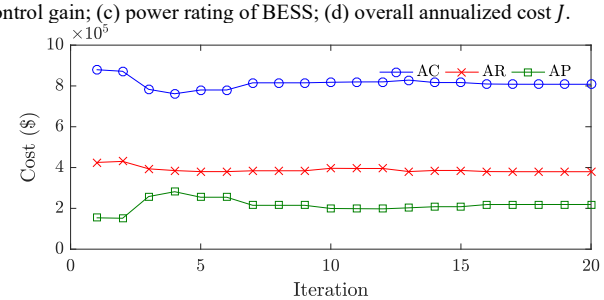

Fig. 11. Outcome of PSO search on the annualized capital cost of the BESS, annualized replacement cost of the BESS, and the annualized penalty cost.

In order to verify the obtained solution is indeed the global optimum, a series of simulation has also been carried out to evaluate the overall annualized cost J using selected ($\bar{P}_{b,\max}$, $\bar{E}_{b0}$) combinations. K_{c0} is then determined by minimizing J using the PSO technique. Fig. 12 shows the relationship between J versus $\bar{E}_{b0}$, for the several $\bar{P}_{b,\max}$ selected. The global optimal result obtained is also shown in the figure. It can be seen that for a given $\bar{P}_{b,\max}$, there is a minimum J and the corresponding BESS capacity $\bar{E}_{b0}^{\text{opt}}$. When $\bar{E}_{b0}$ is less than $\bar{E}_{b0}^{\text{opt}}$, the annualized cost increases rapidly because of the increasingly higher penalty cost due to the mismatched energy and power. For $\bar{E}_{b0}$ above $\bar{E}_{b0}^{\text{opt}}$, the annualized cost increases nearly linearly because there is sufficient stored energy capacity to avoid the penalty, while the annualized cost increases due to the increase in the capital cost of the BESS. Similarly, for each $\bar{E}_{b0}$, there exists an optimal $\bar{P}_{b,\max}$, above and below which J increases.

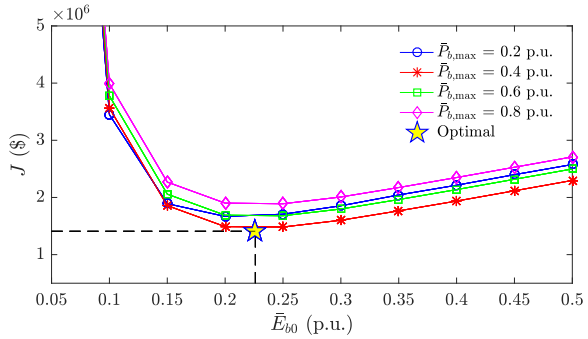

Fig. 12. Relationship between the annualized cost versus BESS energy capacity at different power rating levels.

Fig. 13 shows the relationship between the battery lifetime T_{EOL} versus BESS energy capacity $\bar{E}_{b0}$, for selected BESS power rating $\bar{P}_{b,\max}$. As expected, with an increase in the BESS capacity, the battery lifetime can be prolonged as the current rate will be reduced for individual cell. On the other hand, an increase in the BESS power rating beyond about 0.4 p.u. does not result in significant reduction in the battery lifetime. This is because in this example, the occurrence of battery power higher than 0.4 p.u. is rarely seen. Calendar life of a battery is defined as the battery lifetime under no load condition. Hence, the calendar life of the particular BESS considered in this example is seen to be about 9.3 years when one extrapolates the results shown on Fig. 13 to the condition of $\bar{P}_{b,\max}$ approaches zero while $\bar{E}_{b0}$ is very high. In the course of undertaking the dispatch control task, however, the lifetime of the optimally designed BESS has been reduced to some 7.6 years.

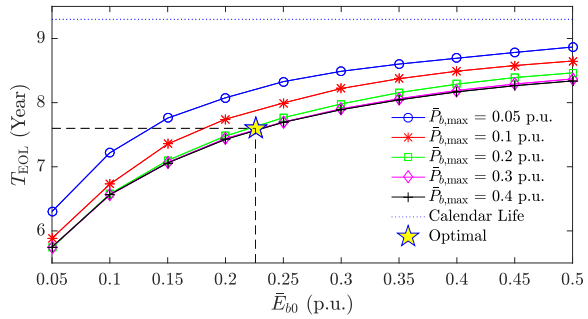

Fig. 13. Relationship between battery lifetime T_{EOL} versus BESS capacity $\bar{E}_{b0}$ at selected power ratings.

6. Conclusions

The present study has developed a planning methodology for determining the capacity of lithium-ion (Li-ion) battery energy storage system (BESS) which is tasked to realize the dispatchability of a renewable power plant. In order to evaluate the impact of the side reactions-induced degradation of the BESS on the intended task, a general second-order power flow model (PFM) of the Li-ion batteries has been developed based on the electrochemical principles of Li-ion cell. The long-term performance and lifetime of the BESS can be more accurately predicted as the BESS undertakes the power dispatch control function. By considering the de-stabilizing actions of the delays introduced by power market rules, bounds have been established on the gain setting of the developed BESS state of energy control scheme. The proposed technique to adaptively adjust the gain setting of the new battery management scheme will prevent the overcharge or overdischarge of the BESS. Annualized capital cost of the battery system is then weighted against the penalty cost when the dispatch power commitment is violated. The optimal BESS stored energy capacity and power rating are then simultaneously determined using a modified particle swarm optimization algorithm, while the stability of the feedback control process to effect adjustments in the dispatch schedule is guaranteed. The proposed methodology therefore provides a general and flexible framework for system-level planning study of minimum-cost BESS design. Numerical examples used to illustrate the proposed design approach show that for a hypothetical 100-MW wind farm to achieve hourly-constant power dispatchability, it requires the incorporation of a 31-MW/22.6-MWh Li-ion BESS into the RE-BESS power plant.

Acknowledgments

This work was supported by Natural Science Foundation of China [grant number: 61703318], the Australian Research Council Discovery Grant [grant number: DP160101325], and the Major Projects of Technical Innovation in Hubei Province [Grant No. 2018AAA050]

Appendix A

From [28], the continuous-time dynamic model of the physics-based ECM shown in Fig. 2 is governed by

$$\dot{Q}_1^{\pm}(t) = C_1^{\pm}\dot{V}_1^{\pm}(t) = I_1^{\pm}(t) \tag{A.1}$$

$$V_{\mathrm{bat}}(t) = V_1^{+}(t) + R_1^{+}I_1^{+}(t) - \left[V_1^{-}(t) + (R_1^{-} + R_f)I_1^{-}(t)\right] \tag{A.2}$$

$$I_1^{+}(t) = I_{\mathrm{bat}}(t) \tag{A.3}$$

$$I_1^{-}(t) = -I_{\mathrm{bat}}(t) - I_{\mathrm{sr}}(t) \tag{A.4}$$

$$V_1^{\pm} = f_{V1}^{\pm}(Q_1^{\pm}) \tag{A.5}$$

$$R_1^{\pm} = f_{R1}^{\pm}(Q_1^{\pm}) \tag{A.6}$$

$$I_{\mathrm{sr}} = f_{\mathrm{Isr}}(Q_1^{-}, I_{\mathrm{bat}}) < 0 \tag{A.7}$$

$$\dot{R}_f(t) = -K_f I_{\mathrm{sr}}(t) \tag{A.8}$$

With symbol "±", each of (A.1), (A.5) and (A.6) represents two equations: one for positive electrode (denoted by the symbol "+") and one for the negative electrode (denoted by the symbol "–"). $V_1^{\pm}$, $R_1^{\pm}$, and I_{sr} are expressed as nonlinear functions of the state variables $Q_1^{\pm}$ and the input variable I_{bat}.

The functional relationships $f_{V1}^{\pm}$, $f_{R1}^{\pm}$ and $f_{\mathrm{Isr}}^{\pm}$ can be determined from the electrochemical characteristics of the electrode materials. Furthermore, in the present investigation, the main findings following the analysis given in [28] can be summarized as follows.

The resistances can be expressed as

$$R_1^{+} = \overbrace{\frac{1}{2A}\left(\frac{L^{+}}{\kappa_{\mathrm{eff}}^{+}} + \frac{2L^{\mathrm{sep}}}{\kappa_{\mathrm{eff}}^{\mathrm{sep}}} + \frac{L^{-}}{\kappa_{\mathrm{eff}}^{-}}\right)}^{\text{Electrolyte}} + \overbrace{\frac{-f'_{\mathrm{OCP+}}(\theta^{+})}{AL^{+}F\varepsilon_s^{+}c_{s,\max}^{+}}\frac{(R_p^{+})^2}{105D_s^{+}}}^{\text{Diffusion}} + \overbrace{\frac{1}{AL^{+}a^{+}}\frac{R_gT}{F}\frac{1}{r_{\mathrm{eff}}^{+}c_{s,\max}^{+}\sqrt{c_e^0\theta^{+}(1-\theta^{+})}}}^{\text{Activation}} \tag{A.9}$$

$$R_1^{-} = \overbrace{\frac{-f'_{\mathrm{OCP-}}(\theta^{-})}{AL^{-}F\varepsilon_s^{-}c_{s,\max}^{-}}\frac{(R_p^{-})^2}{105D_s^{-}}}^{\text{Diffusion}} + \overbrace{\frac{1}{AL^{-}a^{-}}\frac{R_gT}{F}\frac{1}{r_{\mathrm{eff}}^{-}c_{s,\max}^{-}\sqrt{c_e^0\theta^{-}(1-\theta^{-})}}}^{\text{Activation}} \tag{A.10}$$

The physical meaning of the parameters are given in Table A.1. The material-dependent relationship $f_{\mathrm{OCP}\pm}$ between $V_1^{\pm}$ and the normalized concentration $\theta^{\pm}$ are obtained from [41] (for NMC positive electrode) and [28] (for graphite negative electrode):

$$f_{\mathrm{OCP+}}(\theta^{+}) = 6.0826 - 6.9922\theta^{+} + 7.1062(\theta^{+})^2 - 2.5947(\theta^{+})^3 - 0.54549\times10^{-4}\exp(124.23\theta^{+} - 114.2593) \tag{A.11}$$

$$f_{\mathrm{OCP-}}(\theta^{-}) = 0.7222 + 0.1387\theta^{-} + 0.029(\theta^{-})^{0.5} - 0.0172(\theta^{-})^{-1} + 0.0019(\theta^{-})^{-1.5} + 0.2808\exp(0.9 - 15\theta^{-}) - 0.7984\exp(0.4465\theta^{-} - 0.4108) \tag{A.12}$$

Also, the functional relationship f_{Isr} between the negative electrode side-reaction current density J_{sr}, θ^{-} and I_{bat} is assumed known [28]:

$$I_{\mathrm{sr}} = AL^{-}J_{\mathrm{sr}} = AL^{-} \times f_{\mathrm{Jsr}}(\theta^{-}, I_{\mathrm{bat}}) \tag{A.13}$$

Using the expressions (A.14) and (A.15) shown below, substituting $Q_1^{\pm}$ for $\theta^{\pm}$ into (A.9)–(A.13) yields (A.5)–(A.7).

$$\theta^{+}(t) = \theta_{0\%}^{+} - \frac{3600}{AL^{+}F\varepsilon_s^{+}c_{s,\max}^{+}}Q_1^{+}(t) \tag{A.14}$$

$$\theta^{-}(t) = \theta_{100\%}^{-} - \frac{3600}{AL^{-}F\varepsilon_s^{-}c_{s,\max}^{-}}Q_1^{-}(t) \tag{A.15}$$

An example of the relationships between V_{OC}, V_1^{+}, V_1^{-} and the electric charges stored in the capacitors when the battery is

Table A.1
Li-ion battery model parameters for an NMC cell [41].

Symbol	Physical Meaning (Unit)	Parameters		
		Positive Electrode (+)	Separator (sep)	Negative Electrode (–)
R_p	Particle radius (m)	0.7×10^{-6}	-	12.5×10^{-6}
D_s	Solid phase diffusion coefficient ($m^2\cdot s^{-1}$)	8.0×10^{-14}	-	8.8×10^{-14}
a	Specific surface area of electrode (m^{-1})	2.01×10^{6}	-	1.176×10^{5}
L	Thickness of the electrode (m)	165×10^{-6}	30×10^{-6}	103×10^{-6}
ε_s	Volume fraction of the solid phase	0.47	-	0.49
$c_{s,\max}$	Maximum solid phase concentration ($mol\cdot m^{-3}$)	49500	-	30555
$\theta_{0\%}$	Stoichiometry for a fully-discharged battery at BOL	0.735 [a]	-	0.03 [a]
$\theta_{100\%}$	Stoichiometry for a fully-charged battery at BOL	0.39	-	0.89
r_{f0}	Specific SEI film resistance at BOL ($\Omega\cdot m^2$)	0	-	0.001
κ_{eff}	Effective electrolyte conductivity ($S\cdot m^{-1}$)	0.3695	0.2214	0.3445
F	Faraday constant ($s\cdot A\cdot mol^{-1}$)		96487	
T	Battery temperature (K)		298.15	
R_g	Universal gas constant ($J\cdot K^{-1}\cdot mol^{-1}$)		8.314	
c_e^0	Average electrolyte concentration ($mol\cdot m^{-3}$)		1200	
A	electrode plate area (m^2)		0.093 [a]	
Q_{max0}	Ah-capacity at BOL (Ah)		3.3	

a: Re-calibrated for a cell with 3.3 Ah capacity, and voltages at EOC and EOD are 4.2 V and 3.32 V respectively.

at its BOL state is shown by the black solid curves in Fig. A1. The capacity fade can be explained using Fig. A1 as follows:

First, define the EOD state of the battery as that when V_{OC} has reached the pre-specified cut-off voltage level V_{EOD} as indicated in Fig. A1(a). The corresponding amount of electric charges on C_1^+ and C_1^- are denoted as Q_{EOD}^+ and Q_{EOD}^- respectively, as shown in Figs. A1(b) and (c). Similarly, define the EOC state when V_{OC} is V_{EOC}, and Q_{EOC}^+ and Q_{EOC}^- are the corresponding charges on C_1^+ and C_1^-, respectively. The Ah capacity of the battery is $Q_{\max} = Q_{\text{EOD}}^+ - Q_{\text{EOC}}^+ = Q_{\text{EOD}}^- - Q_{\text{EOC}}^-$. In this investigation, the Ah capacity at BOL is denoted as Q_{max0}, with subscript "0" indicating the variable at the BOL, wherein $Q_{\text{EOD0}}^+ = Q_{\text{EOC0}}^- = 0$ and $Q_{\text{EOD0}}^- = Q_{\text{EOC0}}^+ = Q_{\text{max0}}$.

As the battery is put into operation and if one were to ignore the side reactions current, capacitor currents I_1^+ and I_1^- would be identical except that they are in opposite flow directions. So the electric charges Q_1^+ on C_1^+ would change by the amount ΔQ_1^+ which would be exactly matched by the change ΔQ_1^- in the amount of charges Q_1^- on C_1^-. This is reflected by the changes in the operating points A to A′ on the positive electrode, and B to B′ on the negative electrode on the black curves in Figs. A1(b) and (c) during a battery discharging process.

The presence of Q_{loss} can be incorporated into Fig. A1 by shifting the horizontal axis of the OCP vs Q_1^- diagram to the right by an amount of Q_{loss}, with respect to the horizontal axis of the OCP vs Q_1^+ diagram. The new OCV vs. Q_1^+ curve, with the irreversible loss of charges included, is indicated by the red curve in Fig. A1(a). The new OCV curve intersects the battery terminal voltage limit lines V_{EOD} and V_{EOC} to yield the revised Q_{EOC}^+ and Q_{EOD}^+ values shown there. It can be seen from the figure that Q_{EOD}^+ tends to shift more to the right than Q_{EOC}^+, which therefore clearly reflects a reduction in the storage Ah capacity of the battery.

Taking the time derivative of (2) and using (A.1), (A.3), and (A.4) yields

$$\dot{Q}_{\text{loss}}(t) = \dot{Q}_1^+(t) + \dot{Q}_1^-(t) = -I_{\text{sr}}(t) \tag{A.16}$$

Equation (A.16) indicates that the capacity fade is the result of the presence of the side reactions current I_{sr}. In fact, the side reactions culminate in the growth of the SEI layer in the electrode, which then appears in the ECM in the form of the SEI resistance R_f shown in (A.8). Using (A.8) and (2), R_f can be express as

$$R_f(t) = R_{f0} + K_f Q_{\text{loss}}(t) \tag{A.17}$$

where $R_{f0} = r_{f0}^-/(AL^-a^-)$ is the SEI resistance at the BOL. Therefore, it can be seen that R_f is a linear function of Q_{loss} and in view of (2), R_f is in turn a dependent variable of the state variables $Q_1^\pm$. Hence, this ECM is a second-order system.

Appendix B

The amount of stored energy E_1 (in Wh) in a battery cell is given by the difference in the energies stored on C_1^+ and C_1^-, as the two capacitors are series-connected but with the opposite polarity. Since the battery has been prevented from operating when its terminal voltage is below V_{EOD}, one could define $E_1 = 0$ at the EOD state. Hence for any given Q_1^+ and Q_1^-,

$$\begin{aligned} E_1(Q_1^+, Q_1^-) &= E_1^+(Q_1^+) - E_1^-(Q_1^-) \\ &= \int_{Q_{\text{EOD}}^+}^{Q_1^+} V_1^+(Q_1^{+\prime})dQ_1^{+\prime} - \int_{Q_{\text{EOD}}^-}^{Q_1^-} V_1^-(Q_1^{-\prime})dQ_1^{-\prime} \end{aligned} \tag{B.1}$$

As $Q_{\text{EOD}}^\pm$ and $Q_{\text{EOC}}^\pm$ can be expressed as functions of Q_{loss} [28] and in view of (2), $Q_{\text{EOD}}^\pm$ and $Q_{\text{EOC}}^\pm$ can in turn be expressed as functions of Q_1^+ and Q_1^- too. Hence in (B.1), E_1 is shown as a function of Q_1^+ and Q_1^-. Furthermore, Q_{loss} is also a function of Q_1^+ and Q_1^- according to (2).

From the circuit structure of the ECM, it can be seen that the stored energy E_1 increases continuously as Q_1^+ increases, as well as when Q_1^- decreases. Hence, by considering (2), it can be seen that the following Jacobian determinant is non-zero, i.e.

$$|\mathbf{J}| = \begin{vmatrix} \dfrac{\partial E_1}{\partial Q_1^+} & \dfrac{\partial E_1}{\partial Q_1^-} \\ \dfrac{\partial Q_{\text{loss}}}{\partial Q_1^+} & \dfrac{\partial Q_{\text{loss}}}{\partial Q_1^-} \end{vmatrix} = \begin{vmatrix} \dfrac{\partial E_1}{\partial Q_1^+} & \dfrac{\partial E_1}{\partial Q_1^-} \\ 1 & 1 \end{vmatrix} = \frac{\partial E_1}{\partial Q_1^+} - \frac{\partial E_1}{\partial Q_1^-} > 0 \quad \text{(B.2)}$$

According to inverse function theorem [42], in view of (B.2) and the nonlinear transformation from $(Q_1^+, Q_1^-) \in \mathbb{R}^2$ to $(E_1, Q_{\text{loss}}) \in \mathbb{R}^2$ has unique continuation property, the inverse functions of (2) and (B.1) are guaranteed to exist. Thus Q_1^+ and Q_1^- can be expressed as explicit functions of E_1 and Q_{loss}, i.e.,

$$Q_1^{\pm} = g^{\pm}(E_1, Q_{\text{loss}}) \quad \text{(B.3)}$$

Substituting (B.3) into (A.5)–(A.7) yields

$$V_1^{\pm} = f_V^{\pm} \circ g^{\pm}(E_1, Q_{\text{loss}}) \quad \text{(B.4)}$$

$$R_1^{\pm} = f_R^{\pm} \circ g^{\pm}(E_1, Q_{\text{loss}}) \quad \text{(B.5)}$$

$$I_{\text{sr}} = f_{\text{sr}}(f_V^- \circ g^-(E_1, Q_{\text{loss}}), I_{\text{bat}}) \quad \text{(B.6)}$$

where "$\circ$" is the notation for function composition.

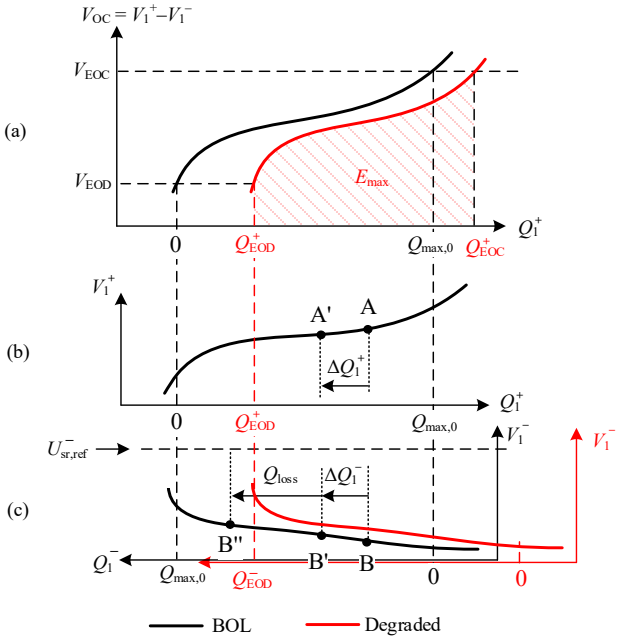

Fig. A1. Typical relationships between OCV, V_1^+, V_1^-, Q_1^+, Q_1^- and Q_{loss}: (a) OCV vs Q_1^+; (b) Positive electrode OCP vs Q_1^+; (c) Negative electrode OCP vs Q_1^-. The black solid curves are pertaining to the cell at the BOL state. Fig. A1 (c) has been shifted along its horizontal axis to the right by an amount Q_{loss} to yield the new plot shown in red to account for the cell degradation. This in turn leads to the phenomenon of capacity fade as reflected by the reduction in the feasible Q_{EOC}^+ to Q_{EOD}^+ operating range in Fig. A1(a), compared to that at the BOL state.

Next, since I_{sr} tends to be much smaller in comparison to I_{bat}, a new parameter η_1 can now be introduced. η_1 is defined as the ratio between the power flow P_1 in the capacitors C_1^+ and C_1^- and the power flow P_{bat} at the battery terminals. With the assumption $I_{\text{sr}} \ll I_{\text{bat}}$, and considering $P_1 = V_{\text{OC}} I_{\text{bat}}$ and $P_{\text{bat}} = P_1 + R_{\text{eq}} I_{\text{bat}}^2$, I_{bat}^2 and η_1 can be expressed as:

$$I_{\text{bat}} = (\sqrt{V_{\text{OC}}^2 + 4R_{\text{eq}}P_{\text{bat}}} - V_{\text{OC}})/(2R_{\text{eq}}) \quad \text{(B.7)}$$

$$\eta_1 = \frac{P_1}{P_{\text{bat}}} = \frac{P_1}{P_1 + R_{\text{eq}} I_{\text{bat}}^2} = 1 - \frac{R_{\text{eq}} I_{\text{bat}}^2}{P_1 + R_{\text{eq}} I_{\text{bat}}^2} \quad \text{(B.8)}$$

where $R_{\text{eq}} = R_1^+ + R_1^- + R_f$, represents the total internal resistance. Clearly, (B.8) indicate that $\eta_1 < 1$ during battery charging ($P_1 > 0$), $\eta_1 > 1$ during battery discharging ($P_1 < 0$), and $\eta_1 = 1$ at no load condition. Noting that the $V_{\text{OC}} = V_1^+ - V_1^-$, and substituting (B.4) and (B.7) into (B.8) and (B.6), η_1 and I_{sr} can then be expressed as functions of the new state variables E_1 and Q_{loss}, and the input P_{bat}. These functions are shown as (4a) and (4b), having taken into consideration of the relationship (A.15).

References

[1] Australian Energy Statistics, Table O. Department of the Environment and Energy; 2019.

[2] Khalid M, Aguilera RP, Savkin AV, Agelidis VG. On maximizing profit of wind-battery supported power station based on wind power and energy price forecasting. Appl Energy. 2018;211:764-73.

[3] Luo X, Wang J, Dooner M, Clarke J. Overview of current development in electrical energy storage technologies and the application potential in power system operation. Appl Energy. 2015;137:511-36.

[4] Xue N, Du W, Greszler TA, Shyy W, Martins JRRA. Design of a lithium-ion battery pack for PHEV using a hybrid optimization method. Appl Energy. 2014;115:591-602.

[5] Scopelianos S, Fedorowytsch T, Garcia S. Elon Musk's Tesla to build world's biggest lithium ion battery to secure power for South Australia. ABC News2017.

[6] Li X, Hui D, Lai X. Battery energy storage station (BESS)-based smoothing control of photovoltaic (PV) and wind power generation fluctuations. IEEE Trans Sustain Energy. 2013;4:464-73.

[7] Zhang F, Meng K, Xu Z, Dong ZY, Zhang L, Wan C, Liang J. Battery ESS planning for wind smoothing via variable-interval reference modulation and self-adaptive SOC control strategy. IEEE Trans Sustain Energy. 2017;8:695-707.

[8] Yang Y, Li H, Aichhorn A, Zheng J, Greenleaf M. Sizing strategy of distributed battery storage system with high penetration of photovoltaic for voltage regulation and peak load shaving. IEEE Trans Smart Grid. 2014;5:982-91.

[9] Bai L, Jiang T, Li F, Chen H, Li X. Distributed energy storage planning in soft open point based active distribution networks incorporating network reconfiguration and DG reactive power capability. Appl Energy. 2018;210:1082-91.

[10] Jannesar MR, Sedighi A, Savaghebi M, Guerrero JM. Optimal placement, sizing, and daily charge/discharge of battery energy storage in low voltage distribution network with high photovoltaic penetration. Appl Energy. 2018;226:957-66.

[11] Kumar A, Meena NK, Singh AR, Deng Y, He X, Bansal RC, Kumar P. Strategic integration of battery energy storage systems with the provision of distributed ancillary services in active distribution systems. Appl Energy. 2019;253:113503.

[12] Yao DL, Choi SS, Tseng KJ, Lie TT. Determination of short-term power dispatch schedule for a wind farm incorporated with dual-battery energy storage scheme. IEEE Trans Sustain Energy. 2012;3:74-84.

[13] Li Y, Choi SS, Vilathgamuwa DM, Yao DL. An improved dispatchable wind turbine generator and dual-battery energy storage system to reduce battery capacity requirement. 2nd IEEE Southern Power Electronics Conference (SPEC). Auckland, New Zealand: IEEE; 2016. p. 1-6.

[14] Wee KW, Choi SS, Vilathgamuwa DM. Design of a least-cost battery-supercapacitor energy storage system for realizing dispatchable wind power. IEEE Trans Sustain Energy. 2013;4:786-96.

[15] Shim JW, Cho Y, Kim S, Min SW, Hur K. Synergistic control of SMES and battery energy storage for enabling dispatchability of renewable energy sources. IEEE Trans Appl Supercond. 2013;23:5701205-.

[16] Kaabeche A, Bakelli Y. Renewable hybrid system size optimization considering various electrochemical energy storage technologies. Energy Convers Manag. 2019;193:162-75.

[17] Guo S, Liu Q, Sun J, Jin H. A review on the utilization of hybrid renewable energy. Renew Sustain Energy Rev. 2018;91:1121-47.

[18] Li Q, Choi SS, Yuan Y, Yao DL. On the determination of battery energy storage capacity and short-term power dispatch of a wind farm. IEEE Trans Sustain Energy. 2011;2:148-58.
[19] Nguyen C-L, Lee H-H, Chun T-W. Cost-optimized battery capacity and short-term power dispatch control for wind farm. IEEE Trans Ind Appl. 2015;51:595-606.
[20] Luo F, Meng K, Dong ZY, Zheng Y, Chen Y, Wong KP. Coordinated operational planning for wind farm with battery energy storage system. IEEE Trans Sustain Energy. 2015;6:253-62.
[21] Zhang X, Yuan Y, Hua L, Cao Y, Qian K. On generation schedule tracking of wind farms with battery energy storage systems. IEEE Trans Sustain Energy. 2017;8:341-53.
[22] Dufo-López R. Optimisation of size and control of grid-connected storage under real time electricity pricing conditions. Appl Energy. 2015;140:395-408.
[23] Feng X, Sun J, Ouyang M, He X, Lu L, Han X, Fang M, Peng H. Characterization of large format lithium ion battery exposed to extremely high temperature. J Power Sources. 2014;272:457-67.
[24] Ramadass P, Haran B, Gomadam PM, White R, Popov BN. Development of first principles capacity fade model for Li-ion cells. J Electrochem Soc. 2004;151:A196-A203.
[25] Li Y, Vilathgamuwa M, Farrell T, Choi SS, Tran NT, Teague J. A physics-based distributed-parameter equivalent circuit model for lithium-ion batteries. Electrochim Acta. 2019;299:451-69.
[26] Santhanagopalan S, Guo Q, Ramadass P, White RE. Review of models for predicting the cycling performance of lithium ion batteries. J Power Sources. 2006;156:620-8.
[27] Zou C, Manzie C, Nesic D. A framework for simplification of PDE-based lithium-ion battery models. IEEE Trans Control Syst Technol. 2016;24:1594-609.
[28] Li Y, Vilathgamuwa M, Choi SS, Farrell TW, Tran NT, Teague J. Development of a degradation-conscious physics-based lithium-ion battery model for use in power system planning studies. Appl Energy. 2019;248:512-25.
[29] Hesse H, Schimpe M, Kucevic D, Jossen A. Lithium-ion battery storage for the grid-a review of stationary battery storage system design tailored for applications in modern power grids. Energies. 2017;10:2107.
[30] Fortenbacher P, Andersson G. Battery degradation maps for power system optimization and as a benchmark reference. 2017 IEEE Manchester PowerTech. Manchester, UK: IEEE; 2017. p. 1-6.
[31] Yao DL, Choi SS, Tseng KJ. Design of short-term dispatch strategy to maximize income of a wind power-energy storage generating station. IEEE PES Innovative Smart Grid Technologies2011. p. 1-8.
[32] Smith K, Saxon A, Keyser M, Lundstrom B, Ziwei C, Roc A. Life prediction model for grid-connected Li-ion battery energy storage system. American Control Conference (ACC). Seattle, WA, USA: IEEE; 2017. p. 4062-8.
[33] Randall AV, Perkins RD, Zhang X, Plett GL. Controls oriented reduced order modeling of solid-electrolyte interphase layer growth. J Power Sources. 2012;209:282-8.
[34] Wei Z, Zhao J, Xiong R, Dong G, Pou J, Tseng KJ. Online estimation of power capacity with noise effect attenuation for lithium-ion battery. IEEE Trans Ind Electron. 2019;66:5724-35.
[35] Zou C, Klintberg A, Wei Z, Fridholm B, Wik T, Egardt B. Power capability prediction for lithium-ion batteries using economic nonlinear model predictive control. J Power Sources. 2018;396:580-9.
[36] Li Y, Vilathgamuwa DM, Choi SS, Farrell TW, Tran NT, Teague J. Development of control strategy to increase the lifetime of grid-connected Li-ion battery. 5th Int Conf Electr Power Energy Convers Syst (EPECS). Kitakyushu, Japan: IEEE; 2018. p. 1-6.
[37] Raviv D, Djaja EW. Technique for enhancing the performance of discretized controllers. IEEE Control Syst Mag. 1999;19:52-7.
[38] Milano F, Anghel M. Impact of time delays on power system stability. IEEE Trans Circuits Syst I, Reg Papers. 2012;59:889-900.
[39] Poli R, Kennedy J, Blackwell T. Particle swarm optimization. Swarm Intelligence. 2007;1:33-57.
[40] 1-minute Interval Iowa AWOS data.
[41] Awarke A, Pischinger S, Ogrzewalla J. Pseudo 3D modeling and analysis of the SEI growth distribution in large format Li-ion polymer pouch cells. J Electrochem Soc. 2013;160:A172-A81.
[42] Henson MA, Seborg DE. Nonlinear Process Control: Prentice Hall PTR; 1997.